Journal of Magnetism and Magnetic Materials 427 (2017) 325–330

Contents lists available at ScienceDirect

Journal of Magnetism and Magnetic Materials

journal homepage: www.elsevier.com/locate/jmmm

# Tessellated permanent magnet circuits for flow-through, open gradient separations of weakly magnetic materials

Lee R. Moore[a], P. Stephen Williams[b], Jeffrey J. Chalmers[c], Maciej Zborowski[a,*]

[a] Department of Biomedical Engineering, Cleveland Clinic, 9500 Euclid Ave., Cleveland OH 44195, USA
[b] Cambrian Technologies, Inc., Cleveland, OH, USA
[c] William G. Lowrie Department of Chemical and Biomedical Engineering, The Ohio State University, Columbus 151 W. Woodruff Avenue, OH 43210, USA

ARTICLE INFO

*Keywords:*
Magnetic separation
Biomagnetism
Open-gradient magnetic separation
Red blood cell magnetic susceptibility

ABSTRACT

Emerging microfluidic-based cell assays favor label-free red blood cell (RBC) depletion. Magnetic separation of RBC is possible because of the paramagnetism of deoxygenated hemoglobin but the process is slow for open-gradient field configurations. In order to increase the throughput, periodic arrangements of the unit magnets were considered, consisting of commercially available Nd-Fe-B permanent magnets and soft steel flux return pieces. The magnet design is uniquely suitable for multiplexing by magnet tessellation, here meaning the tiling of the magnet assembly cross-sectional plane by periodic repetition of the magnet and the flow channel shapes. The periodic pattern of magnet magnetizations allows a reduction of the magnetic material per channel with minimal distortion of the field cylindrical symmetry inside the magnet apertures. A number of such magnet patterns are investigated for separator performance, size and economy with the goal of designing an open-gradient magnetic separator capable of reducing the RBC number concentration a hundred-fold in 1 mL whole blood per hour.

## 1. Introduction

Magnetic cell separation relies on high magnetic susceptibility contrast between cells tagged with magnetic beads and untagged cells [1]. Conjugation of magnetic beads with cell targeting ligands, typically monoclonal antibodies against cell surface receptors, makes the magnetic cell tagging highly specific to the target cell population. The availability of inexpensive permanent magnets and commercial magnetic cell separators combined with the need for highly sensitive and specific cell separation methods on a preparative scale for diagnostic and therapeutic applications contributed to the wide adoption of the magnetic cell separation method for biomedical and clinical applications [2]. The potential drawback of the method is the reliance on the magnetic labeling reagents that may have an undesirable effect on the target cell biology and may adversely affect downstream cell product processing and molecular analysis for diagnostic applications [3]. In particular, the presence of iron in the analyte is known to interfere with the polymerase chain reaction (PCR) [4]. The issue is even more acute in case of the cell product being intended for therapeutic applications. Here an additional concern is the potential toxicity of unbound, residual magnetic beads in the cell suspension, and in the case of a required untagged cell fraction, the presence of non-specifically bound material in the cell product [5].

The availability of high magnetization saturation ($M_s \approx 1$ T) and high coercive force ($\mu_0 H_c \approx 1$ T) permanent magnets creates opportunities for label-less magnetic cell separation, whereby weak magnetic susceptibility contrast between cell fractions can be compensated by the high magnetic field and high magnetic field gradient of a suitable permanent magnet separator [6]. A prime candidate for such an investigation is the separation of red blood cells (RBCs) from white blood cells (WBCs) because of the high concentration of endogenous iron in the hemoglobin of the RBCs. In the absence of bound oxygen molecules, the hemoglobin is paramagnetic which increases the RBC magnetic susceptibility to a sufficient degree that its magnetic field-induced motion can be distinguished from that of the WBC [7]. The separation of RBCs from WBCs has important practical applications because it is a first step in many analytical and diagnostic applications that require access to pure WBC populations without the RBC interference. Currently, it is accomplished quickly and efficiently by centrifugation or by flash RBC lysis when small blood sample volumes are involved, but those methods have their own disadvantages that make their use problematic in a number of specialized applications [8]. In particular, centrifugation is incompatible with the microfluidic architecture used for lab on a chip fabrication and the flash lysis

* Corresponding author.
*E-mail address:* zborowm@ccf.org (M. Zborowski).

http://dx.doi.org/10.1016/j.jmmm.2016.11.027
Received 26 June 2016; Received in revised form 28 October 2016; Accepted 1 November 2016
Available online 15 November 2016
0304-8853/ 

procedure contaminates the sample with RBC ghosts and free hemoglobin, interfering with downstream molecular analysis. Thus, label-less magnetic RBC and WBC separation may find practical applications in new diagnostic instruments designed for blood analysis [9]. In this study we have concentrated on the question of throughput achievable with the use of commercial permanent magnets for RBC separation from blood.

## 2. RBC throughput model

The separation may be achieved using the quadrupole magnetic field and thin annular channel geometry of the quadrupole magnetic sorter (QMS) [10,11]. The quadrupole field results in a high magnetic field gradient across the thickness of the annular channel. The cell suspension is introduced on a continuous basis adjacent to the inner channel wall with flow rate $Q(a')$ and cell-free fluid introduced to the rest of the channel cross section with flow rate $Q(b')$. The two fluid streams enter the channel on opposite sides of a thin cylinder mounted axisymmetrically within the annular channel inlet. The cylinder serves to smoothly merge the two streams. Under the influence of the magnetic field gradient, deoxygenated RBCs are driven across the channel thickness toward the outer wall as they are carried along the channel length. At the channel outlet the fluid is divided into two streams by a second thin cylinder. One stream is collected from the region close to the inner channel wall and this carries the WBCs that are not influenced by the magnetic field. The other is collected from the region adjacent to the outer wall and this carries the RBCs. By the convention of QMS, these have flow rates of $Q(a)$ and $Q(b)$, respectively.

The merging of the fluid streams at the channel inlet results in a virtual cylindrical surface within the channel dividing fluid elements originating at the two different sources, the position across the channel thickness depending on the ratio of the flow rates. Similarly, the position of the virtual cylindrical surface between fluid elements exiting to each side of the outlet flow splitter depends on the ratio of the outlet flow rates. The positions of these inlet and outlet splitting cylindrical surfaces are easily calculated, and with knowledge of the magnetophoretic mobility of the RBCs as well as the magnetic field and field gradient across the channel, the flow rates for cell separation may be optimized [12]. This theory for optimization shows that the total throughput $TP$, in terms of the number of RBCs removed from a cell suspension, for an array of $N_a$ QMS channels is given by

$$TP = cN_aQ(a') = 2\pi cN_aL\frac{\langle B_o^2\rangle}{\mu_0}\frac{I_2[\rho_i, \rho_{ISS}]}{I_1[\rho_i, \rho_{OSS}]}m_1 \quad (1)$$

where $c$ is the RBC number concentration, $Q(a')$ is the volumetric flow rate of the cell suspension introduced to a single annular channel, $L$ is the axial length of the magnetic field (taken as the vertical dimension of the magnet assembly), $\langle B_o^2\rangle$ the magnitude of the magnetic flux density squared at the inner surface of the outer channel wall (averaged over the array), and $\rho = r/r_o$ is the dimensionless radial coordinate scaled to the annular flow channel outer wall radius, $r_o$ (Table 1). Characteristically, the dependence of throughput on the field gradient does not appear explicitly in Eq. (1), because the quadrupole field is a linear function of the radial coordinate. For a given $\langle B_o^2\rangle$ the field gradient and therefore RBC migration velocity across the channel thickness is inversely dependent on $r_o$. However, for a fixed channel thickness $w$, the channel volume increases with$r_o$, resulting in a slower fluid flow velocity along the channel for fixed volumetric flow rates, almost exactly compensating for the reduced RBC migration velocity. Here $\mu_0 = 4\pi \times 10^{-7}$ Tm/A, and $m_1$ is the critical mobility for an RBC to migrate from the inner channel wall to the outlet virtual splitting surface before exiting the channel. It follows that all RBCs with mobilities greater than or equal to $m_1$ are predicted to exit at outlet $b$ in the $Q(b)$ outlet stream. There are two more terms included in Eq. (1),

**Table 1**
Magnet, magnet array, flow and RBC parameters.

| Parameter | Unit | Value |
|---|---|---|
| Magnet aperture diameter | mm | 9.65 |
| Magnet block dimensions: | mm | |
| width, $b$ | | Variable, see text |
| length, $L$ | | 203.2 |
| thickness | | 4.75 |
| Annulus inner radius, $r_i$ | mm | 3.97 |
| Cylinder outer radius | mm | 4.76 |
| Annulus outer radius, $r_o$ | mm | 4.36 |
| Annular width, $w = r_o - r_i$ | μm | 390 |
| NdFeB N42, $H_c$ | A/m | $9.79\times10^5$ |
| NdFeB N42, $B_r$ | T | 1.30 |
| Total flow rate, $Q$ | mL/min | 0.833 |
| Inlet flow rate ratio, $Q(a')/Q$ | – | 0.20 |
| $\rho_{ISS} = r_{ISS}/r_o$ | – | 0.937 |
| Outlet flow rate ratio, $Q(a)/Q$ | – | 0.25 |
| $\rho_{OSS} = r_{OSS}/r_o$ | – | 0.940 |
| Deoxy RBC magnetophoretic mobility | $mm^3/TAs$ | $(4.17 \pm 2.08)\times10^{-6}$ |
| RBC number concentration | N/mL | $5.0\times10^8$ |

the meaning and origin of which may be fully understood by referring to the original derivation of the theory [12]. The term $I_1[\rho_i, \rho_{OSS}]$ is the solution to an integral associated with RBC trajectory within the annular channel from initial to final radial positions (both rendered dimensionless by division by the radius of the outer wall $r_o$), in this case from the inner channel wall $\rho_i = r_i/r_o$ to the outlet splitting surface $\rho_{OSS} = r_{OSS}/r_o$. The term $I_2[\rho_i, \rho_{ISS}]$ is the solution to an integral associated with calculation of volumetric flow rate between two limits in $\rho$, in this case for the $Q(a')$ flow stream between $\rho_i$ and the inlet splitting surface at $\rho_{ISS} = r_{ISS}/r_o$. These are given by

$$I_1[\rho_i, \rho_{OSS}] = [4\ln\rho - 2\rho^2 + 2A_2(\ln\rho)^2]_{\rho_i}^{\rho_{OSS}}$$
$$I_2[\rho_i, \rho_{ISS}] = [2\rho^2 - \rho^4 + 2A_2\rho^2\ln\rho - A_2\rho^2]_{\rho_i}^{\rho_{ISS}} \quad (2)$$

in which $A_2 = (1 - \rho_i^2)/\ln(1/\rho_i)$.

The tessellation study was designed to explore the influence of both the number of flow channels of fixed dimensions (arranged in regular square arrays) and the dimensions of the magnets between the channels on the predicted RBC sorting throughput. The decrease of magnet size increases the density of the channels in the cross sectional area of the magnet array but may adversely affect throughput because of the expected decrease in value of the parameter $\langle B_o^2\rangle$. This is illustrated in Fig. 1 which shows four different flow channel arrays ($N_a$=1, 4, 9, and 16) and three different magnet block widths ($b$=25.4 mm, 12.7 mm and 6.35 mm, with the other two dimensions held constant, see Table 1, designated Quad 1, Quad 2, and Quad 3, respectively). The concomitant decrease of the magnetic field $B_o$ at the outer channel wall with decreasing size of the magnet blocks (with the flow channel diameter held constant) is illustrated in Fig. 2. To simplify the analysis, the inlet and outlet flow rate ratios were held constant, fixing $\rho_{ISS}$ and $\rho_{OSS}$, and the other, unrelated parameters, including cell parameters ($m_1$, $c$) and the channel geometry ($L$, $\rho_i$) were grouped into a constant $K$, and the throughput, $TP$, was calculated by varying only parameters $N_a$ and $\langle B_0^2\rangle$ The results are reported as the normalized throughput, $TP'$ with respect to parameter $K$:

$$K \equiv \frac{2\pi cLm_1}{\mu_0}\frac{I_2[\rho_i,\rho_{ISS}]}{I_1[\rho_i,\rho_{OSS}]}$$
$$TP = N_a\langle B_o^2\rangle K$$
$$TP' = TP/K = N_a\langle B_o^2\rangle \quad (3)$$

where the normalized throughput, $TP'$, has dimensions of tesla$^2$ ($T^2$). The results are also reported as the ratio of $TP'$ to the surface, $S$ tessellated by the magnets, $TP'/S$ (in $T^2/m^2$) that is a measure of efficiency of such a tessellated magnet design.

The distribution of the RBC at the sorter outlet was calculated by

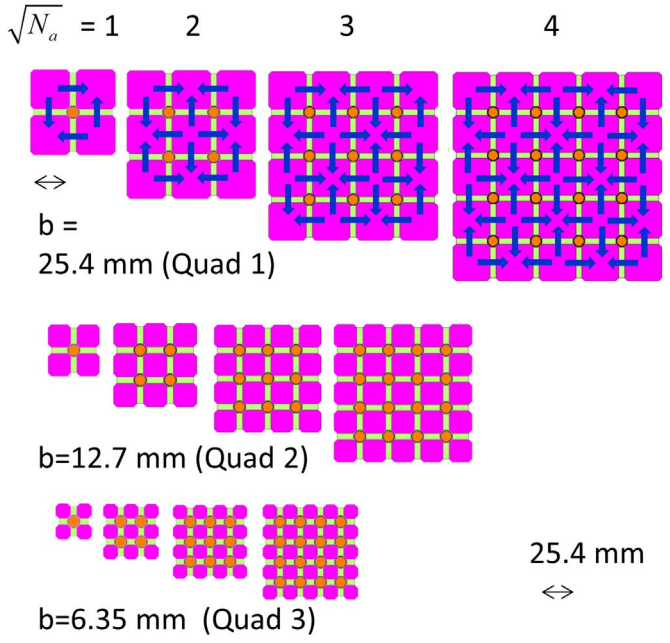


**Fig. 1.** Square magnet array created by tiling with permanent magnet blocks (light rectangles), soft steel yokes (pink) and flow channels (circles). Arrows indicate permanent magnet magnetization directions. Note that as the number of channels to a side increases, $\sqrt{N_a}$=1,.. 4 the average number of magnets per channel decreases 4, ... ~2.5, respectively, and as the width of the permanent magnet decreases $b$=25.4 mm (Quad 1), $b$=12.7 mm (Quad 2) and $b$=6.35 mm (Quad 3), so does the size of the array (at the flow channel diameter held constant). (For interpretation of the references to color in this figure legend, the reader is referred to the web version of this article.)

dividing the region between the annular inner wall and the relevant stream surface into a number of equal radial divisions, such as 50. The initial condition was set by seeding the RBC radial positions at the axial position just before the magnetic field acts, at $z$=0. The RBC trajectory is the result of the vector sum of the magnetic field-induced radial velocity and the axial convection velocity, assumed equal to the local fluid velocity in the annular channel (no RBC sedimentation was included). The magnetic field-induced RBC velocity was distributed over the set of RBC initial positions based on the deoxygenated RBC population magnetophoretic mobility distribution measured by cell tracking velocimetry (CTV) [7]. Approximately 75 pairs of initial RBC positions and mobility values were seeded across the inlet radial range between $\rho_i$ and $\rho_{ISS}$. The radial position of each RBC trajectory terminus was calculated at $z$= $L$ and placed in a bin created by radial divisions of the annulus into fluid flow laminae. The content of each bin is divided by the sum of all the bins to yield fractional RBC recovery across the outlet flow laminae. Different fractional recoveries were calculated for various magnet configurations and plotted using computer algebra software (Maple 17, Maplesoft, Waterloo, ON, Canada).

The magnetic field and field gradient in the annular flow channel inside the magnet aperture was calculated using a commercial software package (2D magnetostatic software Magneto, Integrated Engineering Software, Winnipeg, Canada). A cross-section of the geometry was set up (Fig. 1) with material properties for low carbon steel and permanent magnet NdFeB, 42 MGOe energy product assigned accordingly (Table 1). The polarization of the magnet blocks are shown in the Figs. 1 and 2 to yield quadrupole fields. The geometry was divided into a number of elements ( > 10,000) used by the software for automatic mesh generation. The software then solved the system of differential equations derived from the boundary element method by iteration until

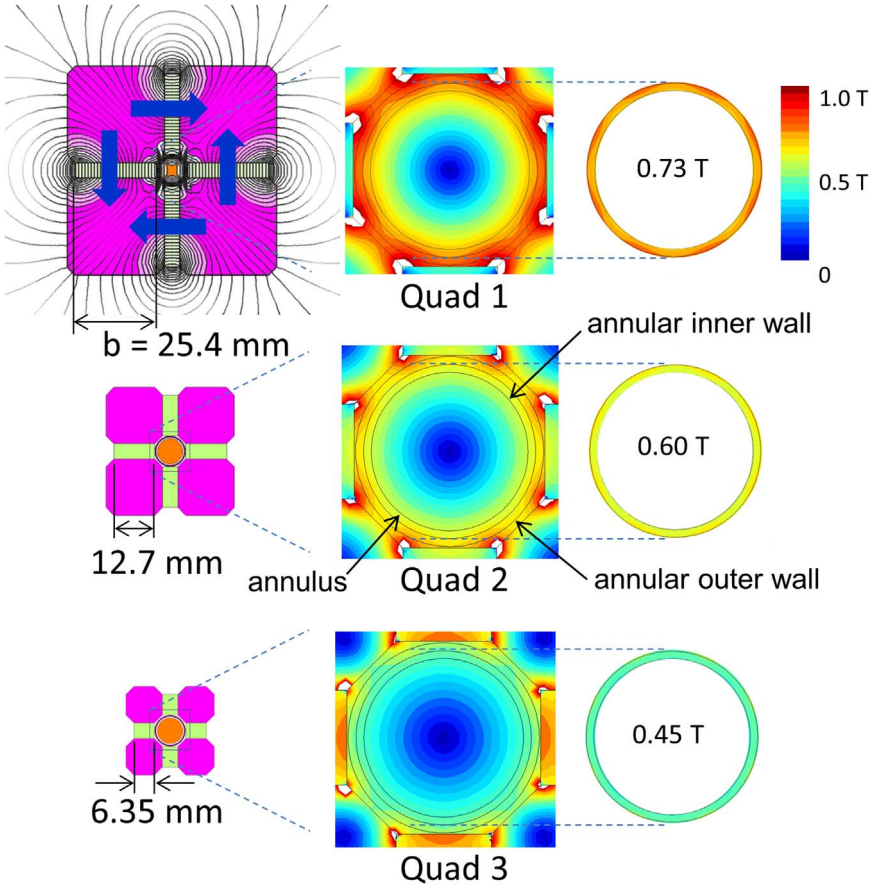


**Fig. 2.** Decreasing magnet block width, $b$ (top to bottom) increases the flow channel number per magnet array cross section area (previous Figure) at a cost of decreasing mean magnetic field over the annular cross section of the flow channel (shown as rings on the right). The middle column shows false color map of the quadrupole field inside the magnet aperture (single unit, in 43.5 mT increments per contour line). (For interpretation of the references to color in this figure legend, the reader is referred to the web version of this article.)

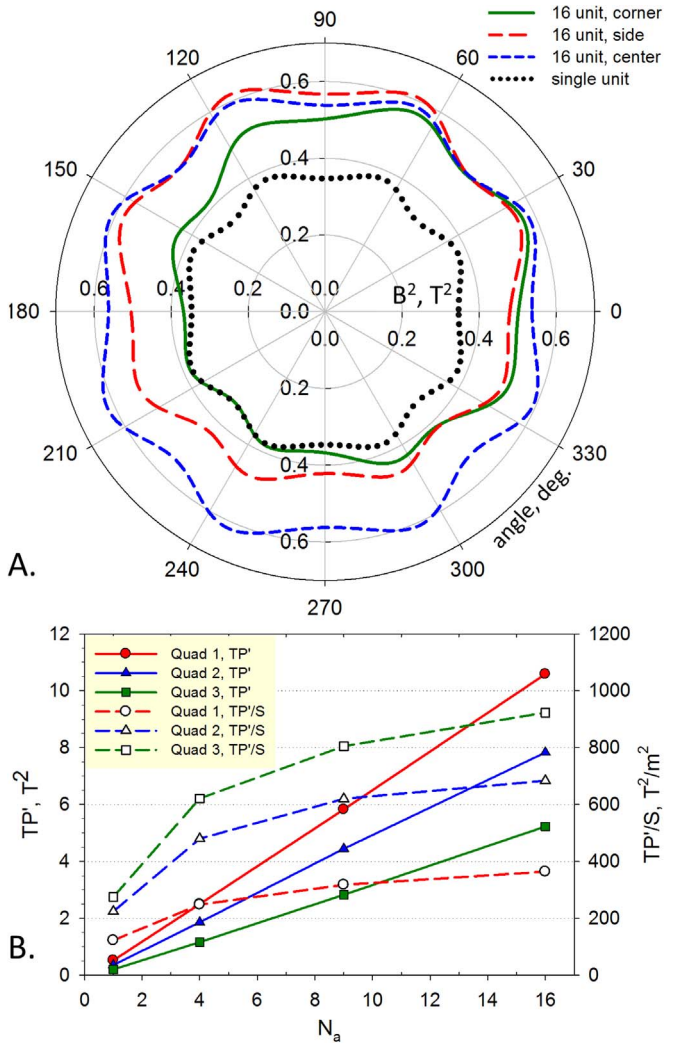


**Fig. 3.** A) Radar plot of $B^2$ field inside a magnet aperture for different aperture locations in the magnet array (see Fig. 1 for center, side and corner aperture positions). Note dependence on the angular coordinate indicating $B^2$ field deviation from an ideal quadrupole field and the dependence on aperture location in the magnet array (most symmetric at the array center and the highest for Quad 1 magnet blocks, 16-channel array). B) Although the throughput per single channel (scaled to magnetostatic potential energy density, proportional to $B^2$) decreases with decreasing magnet block width $b$ (solid lines) the throughput density per magnet array cross section area increases more than 2.5-fold (broken lines). Other symbols are described in text accompanying Eq. (3).

pre-set convergence criteria were met. Computer spreadsheet software (Excel, Microsoft Inc., Redmond, WA) was used to generate a grid at which Magneto evaluates and outputs local values of B field magnitude. These were used to generate field maps and as input matrices used by Maple to solve trajectories, as described above.

## 3. Results and discussion

The feasibility of magnetic RBC separation was first demonstrated using HGMS matrices of soft iron wires [13]. The deflection of deoxygenated RBC in a laminar flow exposed to the magnetic field gradient was visualized and shown to agree with the theoretical predictions based on the RBC magnetic susceptibility [14]. The magnetophoretic mobility of single RBCs and the distribution in mobilities for a sample of thousands of RBCs was measured using cell tracking velocimetry equipped with a (nearly) isodynamic field magnet. The mobilities were shown to agree with susceptibilities of different forms of hemoglobin first reported by Pauling and Coryell in 1936 [7,15]. The random flow patterns in HGMS columns provide little control over the convective cell transport, and their large surface areas promote cell losses due to adhesion resulting in blockages. These aspects generated interest in combining laminar flow in an open rectangular channel with a single wire HGMS [16]. The trade-off is a slower cell sorting speed (throughput, *TP*) compared to the HGMS columns that are, in effect, highly parallel sorting devices. Consequently, access to a high magnetic field is required for the single wire HGMS to operate at realistic throughput levels, available only inside superconducting magnets (up to 6 T) [17,18]. Parallel, single-wire HGMS microfluidic channel systems offer a viable alternative for a typical cell biology laboratory because they are capable of operating at a useful throughput level using permanent magnets with remnant fields of ~1 T [19]. Other means of generating high magnetic gradients using a suitable pattern of flux path elements in combination with parallel microfluidic channels have also been reported [20].

Here we report on an approach that combines an effective use of quadrupole magnetic fields confined to an array of parallel separation channels occupying apertures within a regular pattern of permanent magnet blocks and soft iron flux return elements as shown in Fig. 1. Apart from increasing the throughput, such parallel systems produce a repeating magnetic field pattern that reduces the field losses due to unusable flux return paths and external fringing fields typical of a single channel arrangement (Figs. 1 and 2). In other words, the effective number of magnet blocks per channel decreases with the increasing number of array elements, as can be appreciated by inspection of Fig. 1. Denoting by $N_a$ the number of apertures (equal to the number of flow channels), and by $N_m$ the number of magnet blocks, one obtains for a square magnet array $N_m = 2N_a + 2\sqrt{N_a}$ so that for $N_a$=1 → $N_m$=4, $N_m/N_a = 4$, and for $N_a$=4 → $N_m$=12, $N_m/N_a = 3$, so that in the limit $N_m/N_a \xrightarrow[N_a\to\infty]{} 2$.

Increasing the number of array elements increases the size, and weight, of the compound device and it is therefore natural to consider whether this could be countered by decreasing the size of array elements, without changing the aperture size. The expected reduction in $B_o$ for each aperture leading to a reduction in predicted channel throughput may be more than compensated by the increased number of apertures and channels that may be included in an array of similar mass. For example, the 16-aperture Quad 2 array has a smaller cross sectional area (107.00 mm×107.00 mm) than the 9-aperture Quad 1 array (135.45 mm×135.45 mm) and would have a smaller mass (see Fig. 1). (Note that throughput for an ideal quadrupole field does not depend on the channel diameter but only on its length in the magnetic field as shown by Eq. (1), and the lengths of the arrays are assumed to be fixed at 203.2 mm.) For the three magnet block sizes considered in this study (each differing from the next by a factor of 2 in width $b$, with thickness and length held constant, Table 1) the effective B field and field gradient in the flow channel annulus was indeed found to decrease with the decrease of magnet block size (Fig. 2, single channel quadrupole). In addition to the question of whether the increasing number of the magnet array elements and channels increases the overall throughput sufficiently to counteract the reduction in individual channel throughput due to decreasing $B_o$, it is of interest to determine how much the B field geometry deviates from an ideal quadrupole with the changes in the array size. Such deviations may have an undesirable effect on throughput.

Increasing the number of array elements increased the value of $\langle B_o^2 \rangle$ as compared to a single channel quadrupole as shown in Fig. 3A for the example of a single aperture and 16-aperture Quad 2. Fig. 3B shows that the single aperture Quad 2 has a normalized throughput *TP′* of 0.36 $T^2$ whereas the 16-aperture Quad 2 has a *TP′* of 7.8 $T^2$, which is almost 22 times rather than 16 times higher. This is due to the increasing field contribution from the neighboring elements. The field deviations from an ideal quadrupole were most pronounced for the apertures located at the periphery of the magnet array, as expected (see Fig. 3A). Regarding the question of throughput for fixed mass of array

elements or cross sectional area, the 4-aperture Quad 1, 9-aperture Quad 2, and 16-aperture Quad 3 arrays have decreasing cross sectional areas (100.40 mm, 84.65 mm, and 75.25 mm along their sides, respectively, and as shown in Fig. 1, yet their $TP'$ show an increasing trend in Fig. 3B. The advantage of the larger arrays can be also illustrated by plotting "normalized throughput density", $TP'/S$, defined as the normalized throughput divided by the array cross-sectional area, in $T^2/m^2$, as a function of $N_a$. These are plotted for Quad 1, 2, and 3 as open symbols and dashed lines in Fig. 3B, referring to the right hand axis. In each case, the normalized throughput density increases with $N_a$.

The magnet array cross section area for Quad 1, $N_a$=1 (65.35 mm along the side) is only a little smaller than that of Quad 3, $N_a$=16 (75.25 mm along the side) (Fig. 1) yet the normalized throughput, $TP'$ is predicted to be 10 times higher for the latter (5.3 $T^2$ as opposed to 0.53 $T^2$, Fig. 3B, uncorrected for the sorted product quality, discussed below). This indicates than an array of smaller magnets and flow channels will produce significantly higher RBC sorting throughput than a single channel and larger magnets of a comparable overall array and channel sizes. The objective is to process 1 mL of whole blood per hour, equivalent to 10 mL of a 10-fold dilution for a feed concentration of $5\times10^8$ RBCs/mL. The feed flow rate for each of the 16 channels must therefore be 0.0104 mL/min with total flow rate per channel of 0.052 mL/min. The normalized throughput per channel corresponds to $\langle B_o^2\rangle$ of 5.3/16=0.33 $T^2$. For the fixed values for $\rho_i$, $\rho_{ISS}$, and $\rho_{OSS}$, as listed in Table 1, we calculate $I_1[\rho_i, \rho_{OSS}]$ to be 0.000264 and $I_2[\rho_i, \rho_{ISS}]$ to be 0.000182. Using Eq. (1), a value of $7.53 \times 10^{-7}$ $mm^3$/TAs is found for $m_1$. A second critical mobility $m_0$ corresponds to an RBC that has sufficient time to migrate only from the ISS to the OSS during its time in the region of the magnetic field gradient. It follows that no RBCs having lower mobility can be eliminated from the WBC suspension [12]. This mobility is given by (Fig. 4)

$$m_0 = m_1 \frac{I_1[\rho_{ISS}, \rho_{OSS}]}{I_1[\rho_i, \rho_{OSS}]} \tag{4}$$

With $I_1[\rho_{ISS}, \rho_{OSS}]$ calculated to be 0.0000518, we obtain $m_0$ of $1.48 \times 10^{-7}$ $mm^3$/TAs. The effectiveness of the RBC depletion is then easily calculated by multiplying the RBC mobility distribution curve by the so-called fractional recovery at each outlet. Fractional recovery in the outlet stream $Q(b)$, designated $F_b$, will be equal to 1.0 for mobilities greater than $m_1$ and zero for mobilities less than $m_0$ with an approximately linear change in $F_b$ between these limits. The fractional recovery in outlet stream $Q(a)$ is represented by $F_a$ and is simply equal to $1 - F_b$,

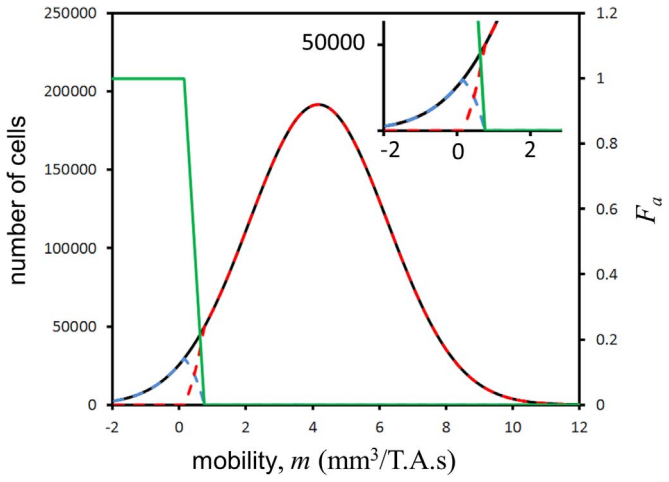


**Fig. 4.** Magnetophoretic mobility distribution (black curve) and cell number predicted to exit with outlet stream $Q(b)$ (removed fraction, red dashed curve) and outlet stream $Q(a)$ (remaining fraction, blue dashed curve). The green step function (referring to the right hand axis) indicates the fractional recovery $F_a$ in the $Q(a)$ stream. The inset shows magnified plot portion for low cell mobility values. (For interpretation of the references to color in this figure legend, the reader is referred to the web version of this article.)

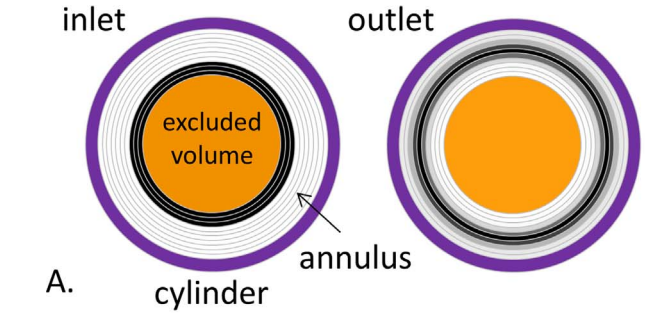


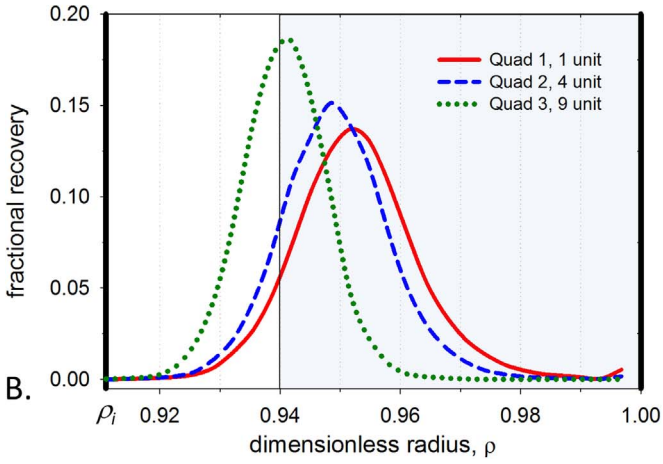


**Fig. 5.** A) RBC number concentration distribution change from the inlet to outlet of the annular flow channel cross-section (averaged over angular position coordinate). Note outward (centrifugal) displacement induced by the magnetic field over the length of the channel. (The annular channel width is exaggerated for illustration purposes.) B) RBC number recovery as a function of dimensionless radial coordinate, $\rho$ at the outlet of the annular flow channel ($\rho_i$ = 0.911 corresponds to the radius of the inner annular channel wall). The shaded area determines the RBC recovery in the outer ("magnetic") fraction beyond $\rho_{OSS}$ = 0.940 for a particular selection of inlet and outlet flow distributions determined from Eq. (1) in text.

provided no RBCs are lost in the channel. The result is shown in Fig. 5. The black Gaussian curve represents the RBC mobility distribution, the dashed red curve shows the fraction carried to outlet stream $Q(b)$, the small dashed blue curve shows the fraction of lower mobility RBCs that remain in the $Q(a)$ stream carrying the WBCs, and the green step function (referring to the right hand axis) represents the variation of $F_a$ with mobility. Integration of the various curves shows that 96.3% of the RBCs are predicted to be removed from the cell suspension. This is very close to the objective of 99%.

The same exercise carried out for a 9-aperture Quad 2 array for which $\langle B_o^2\rangle$=0.50 $T^2$ and feed flow rate $Q(a')$=0.0103 mL/min to each of the 9 channels results in $m_0$ of $1.73 \times 10^{-7}$ $mm^3$/TAs and $m_1$ of $8.79 \times 10^{-7}$ $mm^3$/TAs. At the required throughput 95.9% of the RBCs are predicted to be removed. For a 4-aperture Quad 1 array, $\langle B_o^2\rangle$=0.63 $T^2$, $m_0$=$3.07 \times 10^{-7}$ $mm^3$/TAs, $m_1$=$1.57 \times 10^{-6}$ $mm^3$/TAs, and 93.7% of RBCs are predicted to be removed.

While the reduction in the efficiency of RBC removal may seem small, we can calculate the throughput of whole blood for each case that would be predicted to give the 96.3% RBC removal predicted for the 16 aperture Quad 3 array at 1.0 mL of whole blood per hour. Throughput simply follows $TP'$, so that the 9-aperture Quad 2 array should handle 0.86 mL of blood, the 4-aperture Quad 1 array 0.48 mL, and a single aperture Quad 1 only 0.10 mL of whole blood per hour.

The quality of the RBC separation measured as the RBC recovery in the flow laminae collected at the channel outlet into the "magnetic fraction", for comparable physical dimensions of the magnet arrays

(Fig. 1) was worse for Quad 3, $N_a$=9 (81%) than for Quad 2, $N_a$=4 (91%) and for Quad 1, $N_a$ =1 (95%), Fig. 5B. In other words, the RBC contamination of the "non-magnetic" fraction was 19%, 9%, and 5%, respectively. (Those cells that reach the inner wall of the cylinder are not counted). In order that the quality of the RBC separation for Quad 3, $N_a$=9 array improve to the level of Quad 1, $N_a$=1 configuration, the total flow rate, $Q$ of the former has to decrease. Thus, for the same overall magnet array dimensions, the multiple channel arrangement would generate comparable RBC sorted product as the single channel one, but with an advantage of nearly 5-fold increase in the RBC sorting throughput.

## 4. Conclusions

Surface tessellation with permanent magnet blocks provides convenient means of increasing the efficiency of the magnetic flow cell sorter design by decreasing the mass of magnet blocks per flow channel. For the particular case of the annular flow channels in quadrupole magnetic fields and the same overall tessellated magnet array dimensions, 9- channel array generated a comparable quality of the RBC sorted product as the 1- channel array, but with an advantage of 5-fold higher RBC sorting speed (throughput). The model provides useful guidelines for prototype design and fabrication in application to red blood cell separation for clinical diagnostics limited to 1 mL whole blood sample volumes.

## Acknowledgments

This study was funded by DARPA Project BAA07-21 "Continuous RBC Production" and NIH CA062349.

## References

[1] M. Zborowski, J.J. Chalmers, Rare cell separation and analysis by magnetic sorting, Anal. Chem. 83 (2011) 8050–8056.
[2] A. Grützkau, A. Radbruch, Small but mighty: how the MACS®-technology based on nanosized superparamagnetic particles has helped to analyze the immune system within the last 20 years, Cytom. Part A 77A (2010) 643–647.
[3] U.O. Häfeli, J. Aue, J. Damani, The biocompatibility and toxicity of magnetic particles, in: M. Zborowski, J.J. Chalmers (Eds.), Magnetic Cell Separation, Elsevier, Amsterdam, 2007, pp. 163–223.
[4] Y. Bai, Y. Cui, G.C. Paoli, C. Shi, D. Wang, X. Shi, Nanoparticles affect PCR primarily via surface interactions with PCR components: using amino-modified silica-coated magnetic nanoparticles as a main mode, ACS Appl. Mater. Interfaces 7 (2015) 13142–13153.
[5] J.J. Chalmers, Y. Xiong, X. Jin, M. Shao, X. Tong, S. Farag, M. Zborowski, Quantification of non-specific binding of magnetic micro- and nanoparticles using cell tracking velocimetry: implication for magnetic cell separation and detection, Biotechnol. Bioeng. 105 (2010) 1078–1093.
[6] L.R. Moore, F. Nehl, J. Dorn, J.J. Chalmers, M. Zborowski, Open gradient magnetic red blood cell sorter evaluation on model cell mixtures, IEEE Trans. Magn. 49 (2013) 309–315.
[7] M. Zborowski, G.R. Ostera, L.R. Moore, S. Milliron, J.J. Chalmers, A.N. Schechter, Red blood cell magnetophoresis, Biophys. J. 84 (2003) 2638–2645.
[8] H.M. Shapiro, Practical Flow Cytometry, 4th ed., John Wiley & Sons, Hoboken, NJ, 2005.
[9] N.M. Karabacak, P.S. Spuhler, F. Fachin, E.J. Lim, V. Pai, E. Ozkumur, J.M. Martel, N. Kojic, K. Smith, P.-i. Chen, J. Yang, H. Hwang, B. Morgan, J. Trautwein, T.A. Barber, S.L. Stott, S. Maheswaran, R. Kapur, D.A. Haber, M. Toner, Microfluidic, marker-free isolation of circulating tumor cells from blood samples, Nat. Protoc. 9 (2014) 694–710.
[10] Y. Jing, L.R. Moore, T. Schneider, P.S. Williams, J.J. Chalmers, S.S. Farag, B. Bolwell, M. Zborowski, Negative selection of hematopoietic progenitor cells by continuous magnetophoresis, Exp. Hematol. 35 (2007) 662–672.
[11] K.E. McCloskey, L.R. Moore, M. Hoyos, A. Rodriguez, J.J. Chalmers, M. Zborowski, Magnetophoretic cell sorting is a function of antibody binding capacity, Biotechnol. Progr. 19 (2003) 899–907.
[12] P.S. Williams, M. Zborowski, J.J. Chalmers, Flow rate optimization for the quadrupole magnetic cell sorter, Anal. Chem. 71 (1999) 3799–3807.
[13] D. Melville, F. Paul, S. Roath, High gradient magnetic separation of red cells from whole blood, IEEE Trans. Magn. 11 (1975) 1701–1704.
[14] M. Okazaki, K. Kon, N. Maeda, T. Shiga, Distribution of erythrocyte in a model vessel exposed to inhomogeneous magnetic fields, Physiol. Chem. Phys. Med. NMR 20 (1988) 3–14.
[15] L. Pauling, C.D. Coryell, The magnetic properties and structure of hemoglobin, oxyhemoglobin and carbonmonoxyhemoglobin, Proc. Natl. Acad. Sci. USA 22 (1936) 210–216.
[16] X. Jin, S. Abbot, X. Zhang, L. Kang, V. Voskinarian-Berse, R. Zhao, M.V. Kameneva, L.R. Moore, J.J. Chalmers, M. Zborowski, Erythrocyte enrichment in hematopoietic progenitor cell cultures based on magnetic susceptibility of the hemoglobin, PLoS ONE 7 (2012) e39491.
[17] M. Takayasu, D.R. Kelland, J.V. Minervini, Continuous magnetic separation of blood components from whole blood, IEEE Trans. Appl. Supercond. 10 (2000) 927–930.
[18] J. Svoboda, Separation of red blood cells by magnetic means, J. Magn. Magn. Mater. 220 (2000) L103–L105.
[19] C. Haitao, B. Danny, R. Dietmar, D.K. Michael, J.R. Axel, Three-dimensional modeling of a portable medical device for magnetic separation of particles from biological fluids, Phys. Med. Biol. 52 (2007) 5205–5218.
[20] E.P. Furlani, Magnetophoretic separation of blood cells at the microscale, J. Phys. D: Appl. Phys. 40 (2007) 1313–1319.